

## Supporting Information

for *Adv. Funct. Mater.*, DOI: 10.1002/adfm.202200529

Enhanced Polysulfide Conversion with Highly  
Conductive and Electrocatalytic Iodine-Doped Bismuth  
Selenide Nanosheets in Lithium–Sulfur Batteries

*Mengyao Li, Dawei Yang,\* Jordi Jacas Biendicho, Xu Han, Chaoqi Zhang, Kun Liu, Jiefeng Diao, Junshan Li, Jing Wang, Marc Heggen, Rafal E. Dunin-Borkowski, Jiaao Wang,\* Graeme Henkelman, Joan Ramon Morante, Jordi Arbiol, Shu-Lei Chou,\* and Andreu Cabot\**

## Supporting Information

**Iodine-Doped Bismuth Selenide Nanosheets as effective sulfur host with Enhanced Catalytic Polysulfide Conversion in Lithium-Sulfur Batteries**

*Mengyao Li<sup>+</sup>, Dawei Yang<sup>+\*</sup>, Jordi Jacas Biendicho, Xu Han, Chaoqi Zhang, Kun Liu, Jiefeng Diao, Junshan Li, Jing Wang, Marc Heggen, Rafal E. Dunin-Borkowski, Jiaao Wang\*, Graeme Henkelman, Joan Ramon Morante, Jordi Arbiol, Shu-Lei Chou\*, Andreu Cabot\**

M. Y. Li, D. W. Yang, Dr. J. J. Biendicho, C. Q. Zhang, Prof. J. R. Morante, Prof. A. Cabot  
Catalonia Institute for Energy Research - IREC  
Sant Adrià de Besòs, Barcelona, 08930, Spain  
Email: [acabot@irec.cat](mailto:acabot@irec.cat)

M. Y. Li, D. W. Yang, C. Q. Zhang, Prof. J. R. Morante  
Department of Electronic and Biomedical Engineering  
Universitat de Barcelona, 08028 Barcelona, Spain  
Email: [daweiirec@163.com](mailto:daweiirec@163.com)

X. Han, Prof. J. Arbiol  
Catalan Institute of Nanoscience and Nanotechnology (ICN2)  
CSIC and BIST, Campus UAB, Bellaterra, 08193 Barcelona, Catalonia, Spain

K. Liu  
Institute of Materials and Technology, Dalian Maritime University, Dalian 116026, China

Dr. J. F. Diao, Dr. J. A. Wang, Prof. G. Henkelman  
Department of Chemistry and the Oden Institute for Computational Engineering and Sciences,  
The University of Texas at Austin, Austin, TX, 78712 USA  
Email: [wangjiaao0720@utexas.edu](mailto:wangjiaao0720@utexas.edu)

Dr. J. Li  
Institute of Advanced Study, Chengdu University, 610106  
No. 2025, Chengluo Avenue, Chengdu, Sichuan Province, China

J. Wang  
State Grid Anhui Ultra High Voltage Company, 231100  
No. 8, Jincui Road, Changfeng County, Hefei, Anhui Province, China

Dr. M Heggen, Prof. R E. Dunin-Borkowski  
Ernst Ruska-Centre for Microscopy and Spectroscopy with Electrons and Peter Grünberg  
Institute Forschungszentrum Jülich GmbH 52425 Jülich, Germany

Prof. S. L. Chou  
Institute for Carbon Neutralization, College of Chemistry and Materials Engineering,  
Wenzhou University, Wenzhou, Zhejiang 325035, China

E-mail: [chou@wzu.edu.cn](mailto:chou@wzu.edu.cn)

Prof. J. Arbiol, Prof. A. Cabot  
ICREA

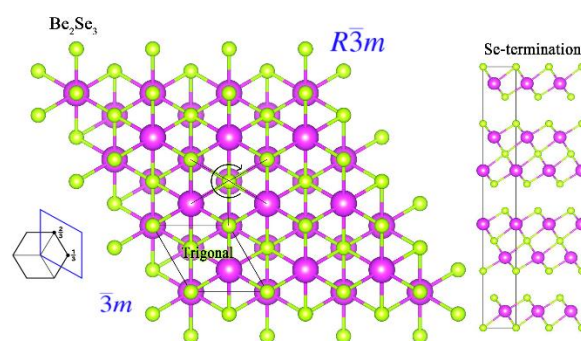
Pg. Lluís Companys 23, 08010 Barcelona, Catalonia, Spain

+ These authors contributed equally to this work

\* Corresponding authors

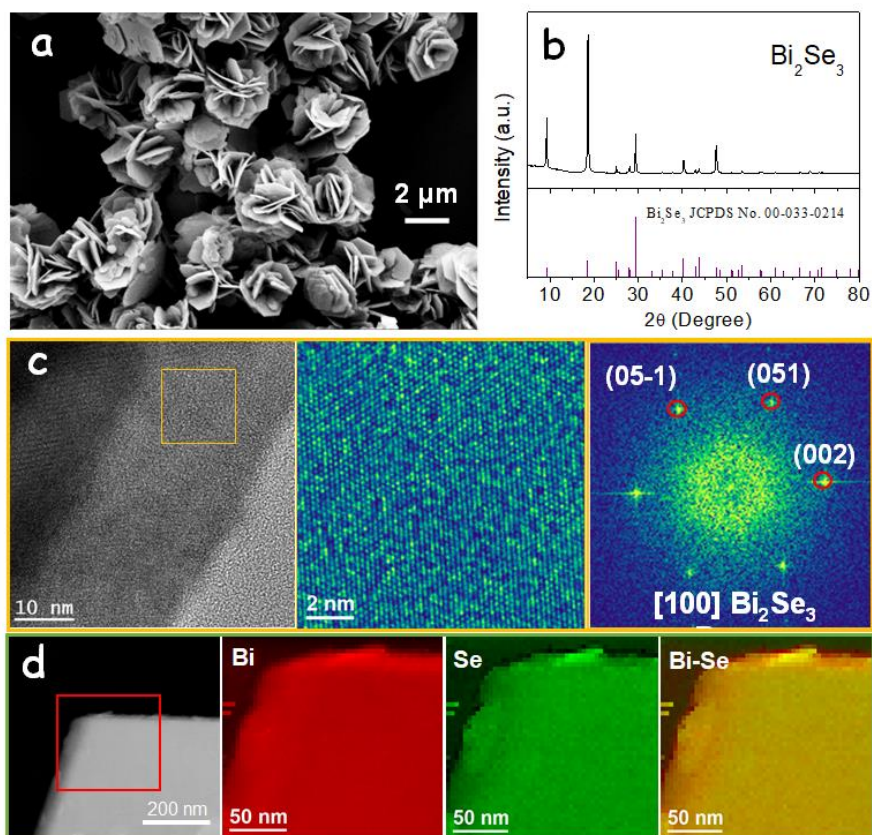
### Details of Theoretical calculations

The most important parameters for Li-S batteries are the LiPS-electrode binding energy as well as the conversion free energy for LiPS on the specific surface. To explain the outstanding performance of our I-doped  $\text{Bi}_2\text{Se}_3$  material used for Li-S electrode, theoretical calculation was employed to offer an electronic-level insight of LiPS's behavior in the working state.  $R\bar{3}m$  Space group XRD simulation patterns of  $\text{Bi}_2\text{Se}_3$  (mp-541837) matches the powder X-ray diffraction patterns well, which was used for further theoretical calculation.

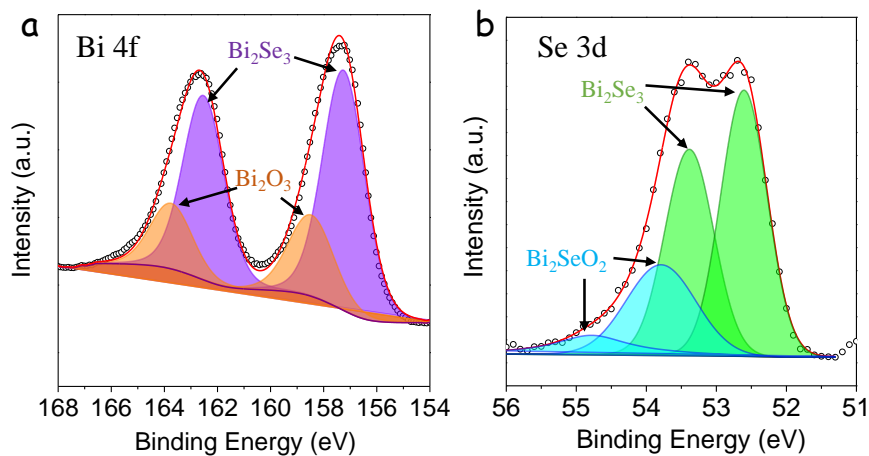


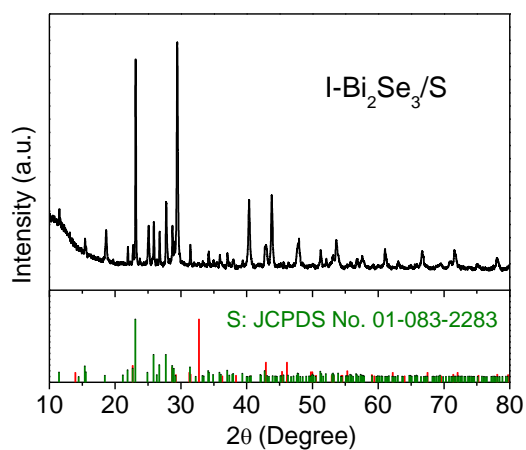
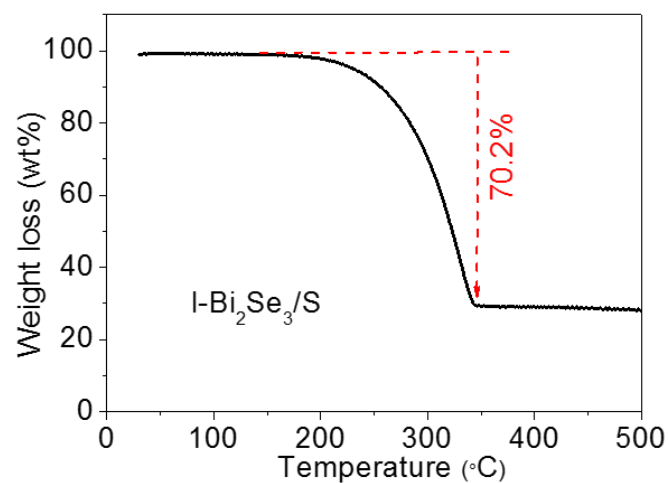
Metal exposed facet can be the most possible active facet, while non-metal element termination always offers a weaker electronic manipulation for the LiPS conversion in most cases.<sup>[1]</sup> So according to the XRD and pre-test of DFT Bader calculation, it was confirmed that  $\text{Bi}_2\text{Se}_3$  (110) plane may be possible the active plane so that it was selected to make a further investigation. Experimental lattice parameters typically not be the minimum, in other words, the most stable state, thus the optimization for atom coordinates and cell was firstly implemented and reached less than 0.05 eV/A stress. Then a  $\text{Bi}_2\text{Se}_3$  (110) slab with 2 nm vacuum layer and I-doped slab were built and optimized with the bottom 2 layers fixed to obtain a more realistic surface electronic structure, for the following LiPS binding energy and conversion free energy. SCAN functional with rVV10 long-distance correction was adopted in the whole energy-involved calculation because SCAN+rVV10 was determined the best combination for describing crystal parameter which in the closet agreement with experimental observation as well as accurate energy presentation exceed that PBE functional family. The

other computation details are the same as our previous work.<sup>1</sup>  $1 \times 2 \times 1$  Monkhorst k-mesh was sampled for each slab model.



**Figure S1.** (a) SEM images of the  $\text{Bi}_2\text{Se}_3$  nanosheets. (b) XRD patterns of  $\text{Bi}_2\text{Se}_3$  nanosheets. (c) HRTEM images of the  $\text{Bi}_2\text{Se}_3$  nanosheets and its corresponding power spectrum. (d) EELS chemical composition maps obtained from the red squared area of the STEM micrograph. Individual Bi  $\text{N}_{2,3}$ -edges at 679 eV (red), Se  $\text{L}_{2,3}$ -edges at 162 eV (green) and composites of Bi-Se.



**Figure S2.** Bi 4f and Se 3d high-resolution XPS spectra.**Figure S3.** XRD pattern of I-Bi<sub>2</sub>Se<sub>3</sub>/S.**Figure S4.** TGA curve of I-Bi<sub>2</sub>Se<sub>3</sub>/S composite measured in N<sub>2</sub> with a sulfur loading ratio of 70.2 wt%.

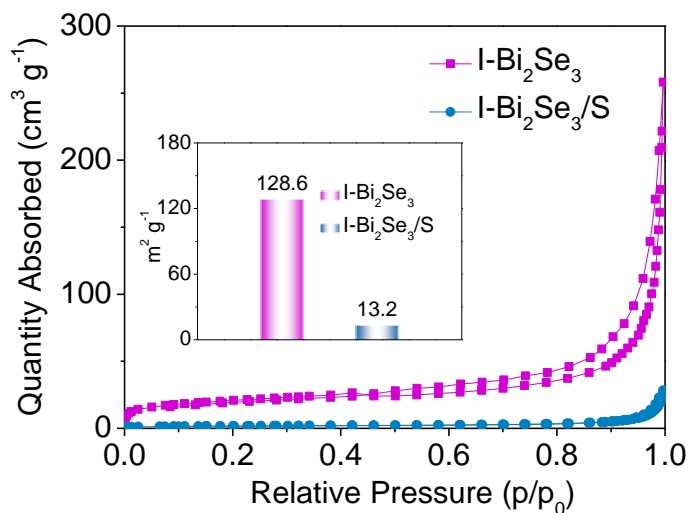


**Figure S5.** Nitrogen adsorption-desorption isotherms of as synthesized I-Bi<sub>2</sub>Se<sub>3</sub> and I-Bi<sub>2</sub>Se<sub>3</sub>/S composites.

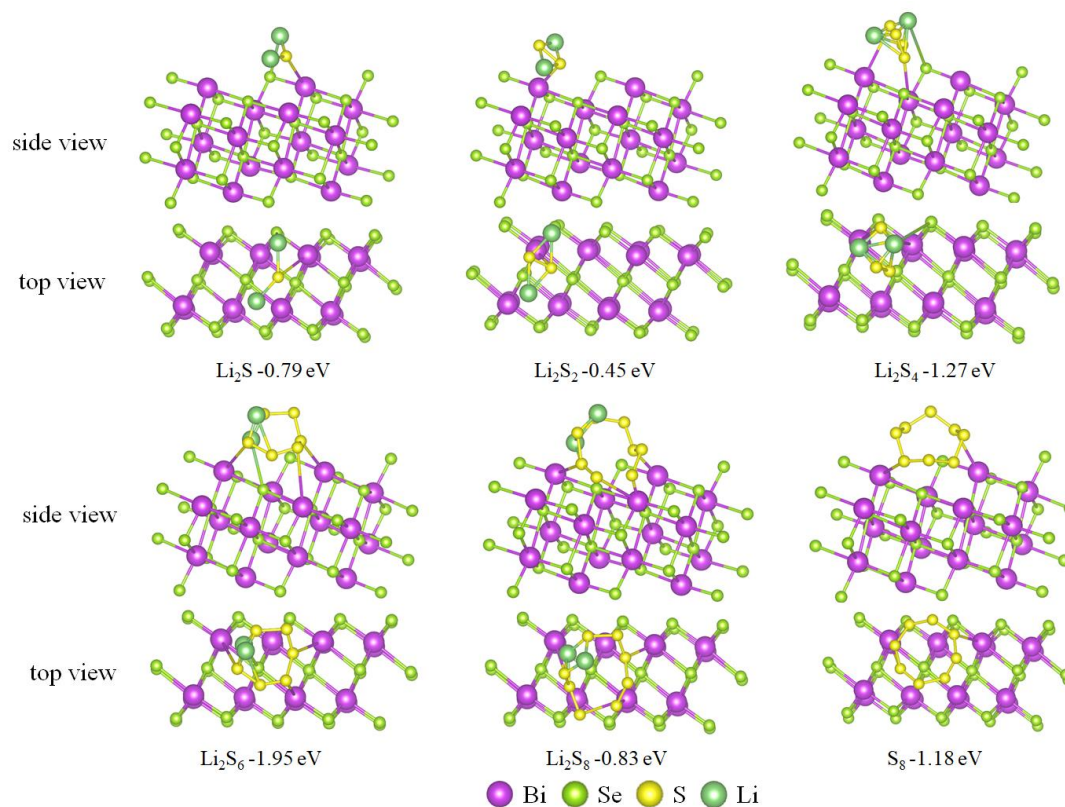


**Figure S6.** DFT calculation results of optimized geometrical configurations of the surface (110) of Bi<sub>2</sub>Se<sub>3</sub> with LiPS (Li<sub>2</sub>S, Li<sub>2</sub>S<sub>2</sub>, Li<sub>2</sub>S<sub>4</sub>, Li<sub>2</sub>S<sub>6</sub>, Li<sub>2</sub>S<sub>8</sub> and S<sub>8</sub>).

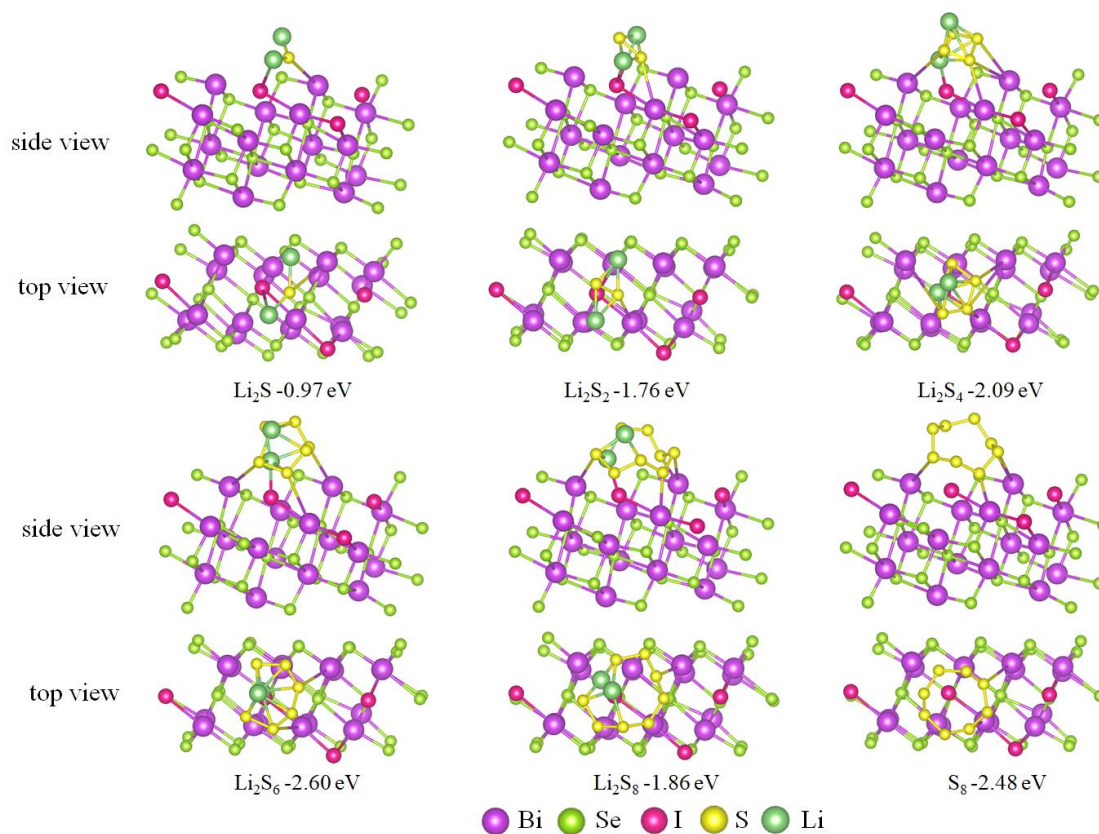


**Figure S7.** DFT calculation results of optimized geometrical configurations of the surface (110) of I-Bi<sub>2</sub>Se<sub>3</sub> with LiPS ( $\text{Li}_2\text{S}$ ,  $\text{Li}_2\text{S}_2$ ,  $\text{Li}_2\text{S}_4$ ,  $\text{Li}_2\text{S}_6$ ,  $\text{Li}_2\text{S}_8$  and  $\text{S}_8$ ).

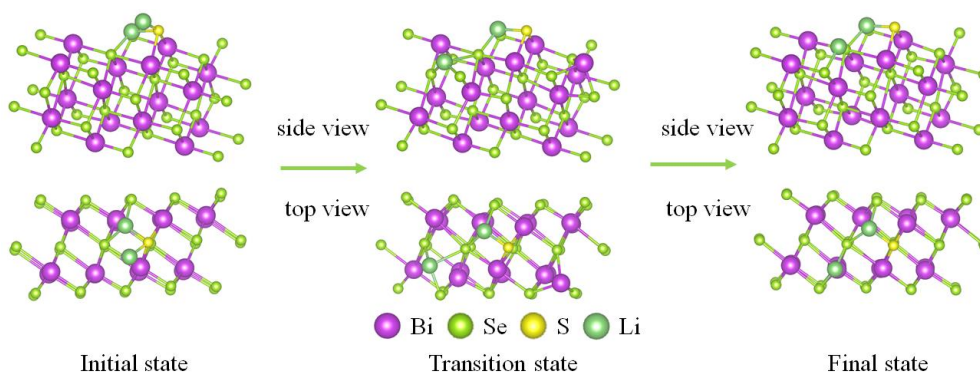


**Figure S8.** Optimized adsorption configuration of  $\text{Li}_2\text{S}$  decomposition on  $\text{Bi}_2\text{Se}_3$ .

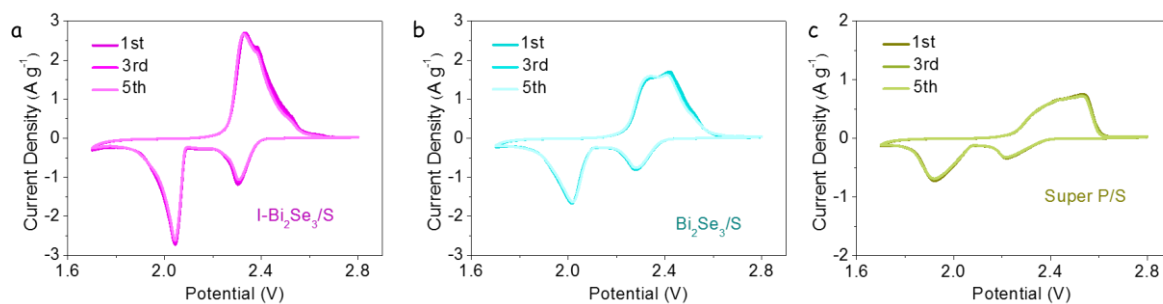


**Figure S9.** First five cycles of CV curves of (a) I-Bi<sub>2</sub>Se<sub>3</sub>/S, (b) Bi<sub>2</sub>Se<sub>3</sub>/S and (c) Super P/S performed at a scan rate of 0.1 mV s<sup>-1</sup>.

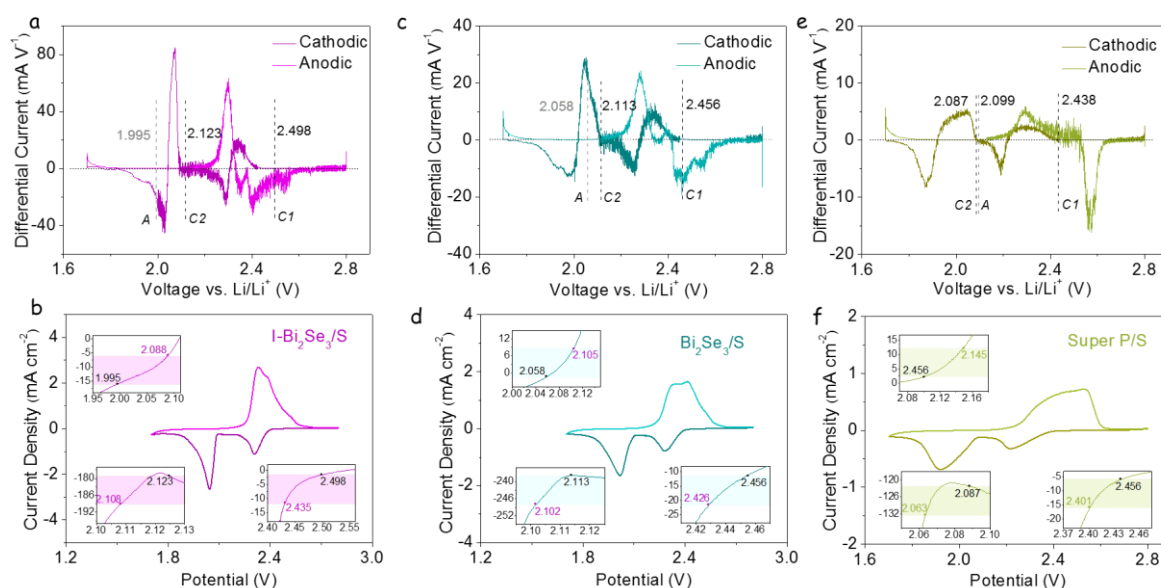


**Figure S10.** Differential CV curves of (a) I-Bi<sub>2</sub>Se<sub>3</sub>/S, (c) Bi<sub>2</sub>Se<sub>3</sub>/S and (e) Super P/S. The baseline voltage and current density are defined as the value before the redox peak, where the variation on current density is the smallest, named as  $dI/dV=0$ . The value of the baseline voltages for cathodic peak C1, C2 and anodic peak A were calculated, respectively. CV curves and corresponding onset potentials of redox peak C1, C2, and A (inset): (b) I-Bi<sub>2</sub>Se<sub>3</sub>/S, (d) Bi<sub>2</sub>Se<sub>3</sub>/S and (f) Super P/S. Following a common definition employed in electrocatalysis, the onset potential is determined when the current density is 10  $\mu\text{A cm}^{-2}$  beyond the corresponding baseline current density (more specifically, 10  $\mu\text{A cm}^{-2}$  more negative than baseline current density for cathodic peaks or 10  $\mu\text{A cm}^{-2}$  positive than baseline current density for anodic peaks). As shown in the inset of b, d, and f, the baseline voltages are the same as in a, c, and e while the colored region indicates the gap in current density.

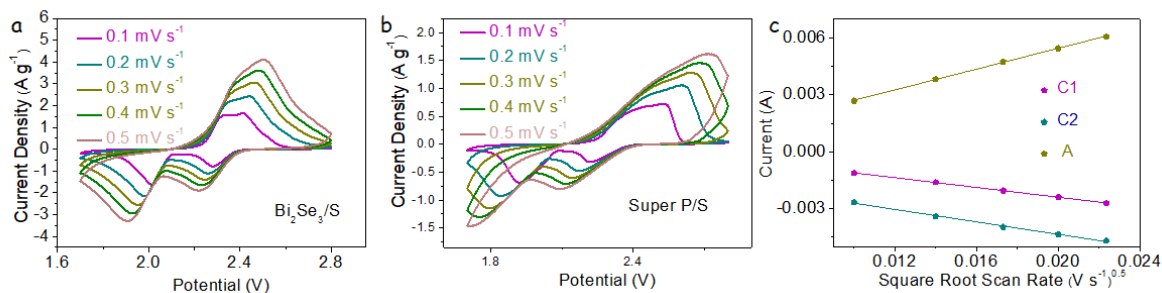


**Figure S11.** CV curves of (a) Bi<sub>2</sub>Se<sub>3</sub>/S, (b) Super P/S and (c) Plot of CV peak current for peaks C1, C2, and A versus the square root of the scan rates.

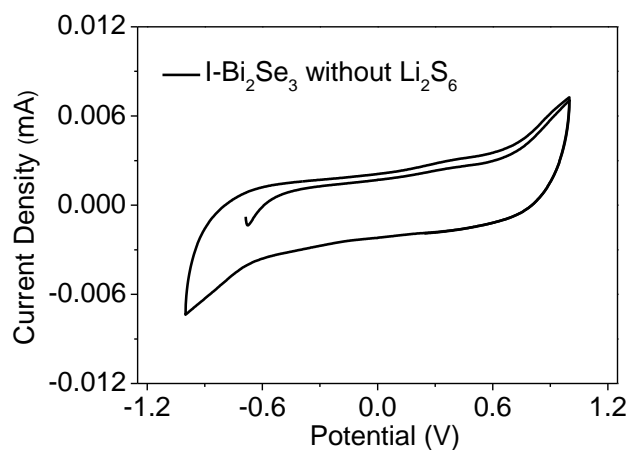


**Figure S12.** The CV curve of I-Bi<sub>2</sub>Se<sub>3</sub> as electrode measured in symmetric coin cell using an electrolyte without Li<sub>2</sub>S<sub>6</sub>.

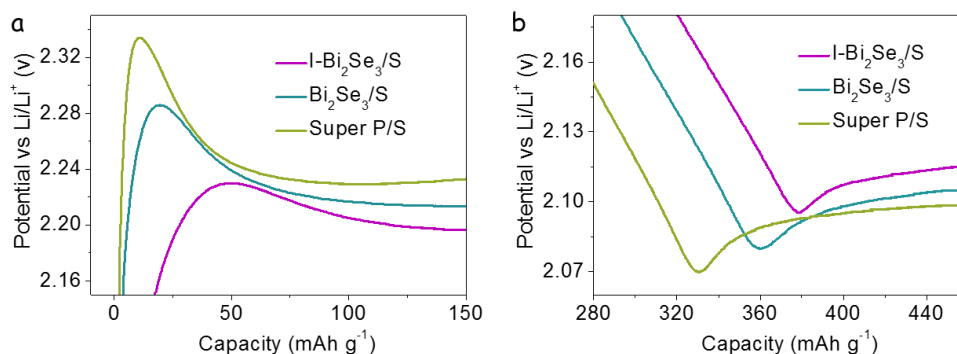


**Figure S13.** (a) Charge, and (b) discharge profiles of I-Bi<sub>2</sub>Se<sub>3</sub>/S, Bi<sub>2</sub>Se<sub>3</sub>/S, and Super P/S electrodes showing the overpotentials for conversion between soluble LiPS and insoluble Li<sub>2</sub>S<sub>2</sub>/Li<sub>2</sub>S.

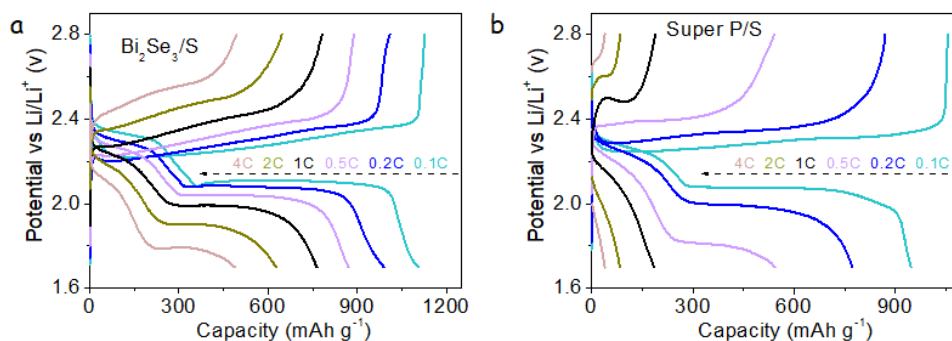


**Figure S14.** Galvanostatic charge–discharge profiles of (a)  $\text{Bi}_2\text{Se}_3/\text{S}$  and (b) Super P/S at different current densities range from 0.1C to 4C.

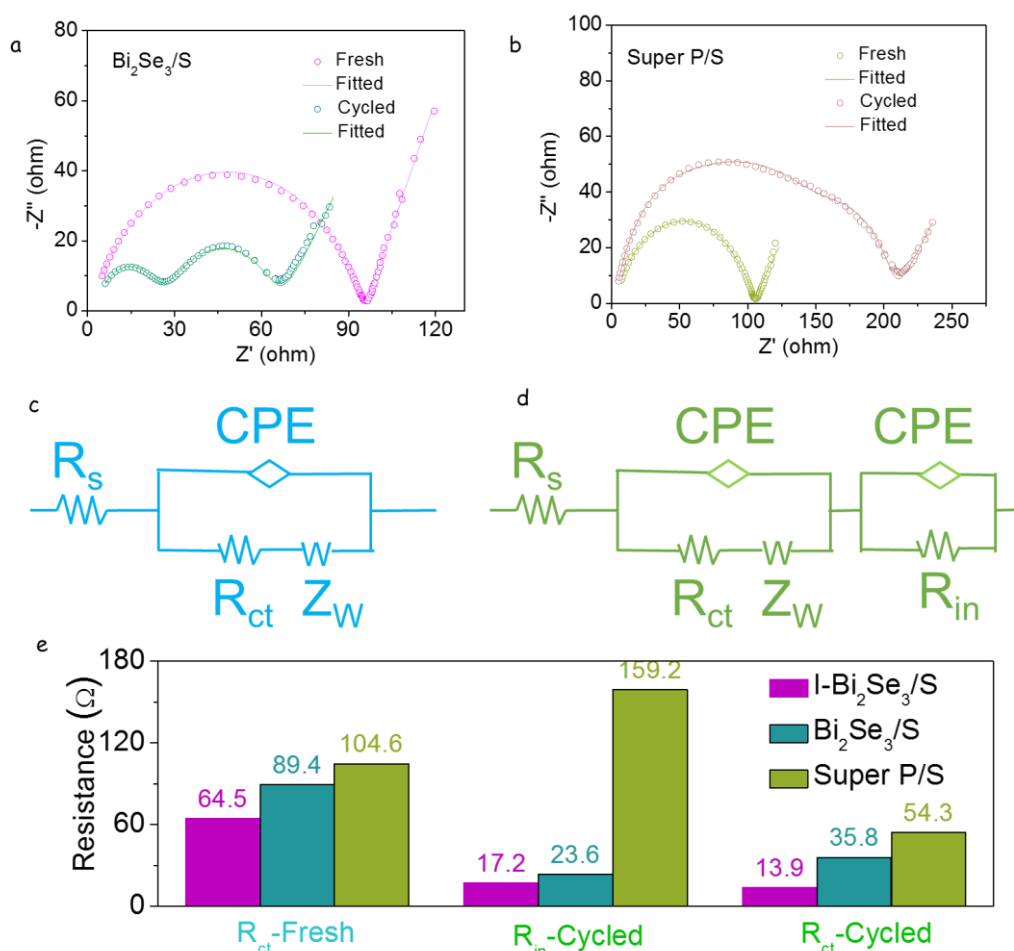


**Figure S15.** (a,b) EIS spectra of (a)  $\text{Bi}_2\text{Se}_3/\text{S}$  and (b) Super P/S coin cells before and after cycling. The solid line corresponding to the fitting result from the equivalent circuit (c) and (d), and the  $R_s$ ,  $R_{in}$ ,  $R_{ct}$ , and  $Z_w$  stand for the resistance of the electrolyte, insoluble  $\text{Li}_2\text{S}_2/\text{Li}_2\text{S}$  layer, interfacial charge-transportation, and semi-infinite Warburg diffusion, respectively; and CPE stands for the corresponding capacitance. (e) Different resistances of three coin cells were obtained from the equivalent circuit.

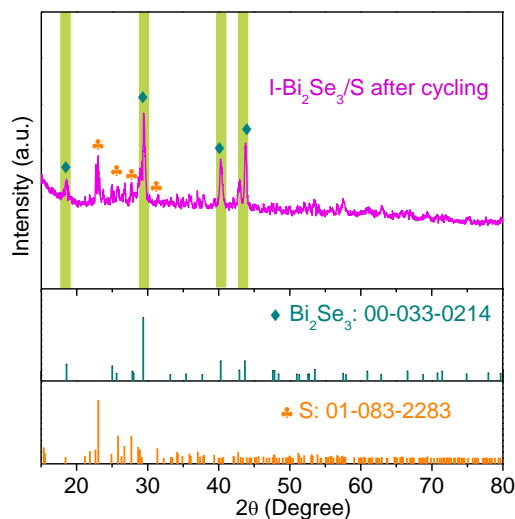


**Figure S16.** XRD patterns of electrode materials after 100 cycles at 1C. After cycling test, the coin cells were charged to 3 V at 0.1 C, and then they were unpacked and washed by DOL/DME solution to remove Li-based salt. After drying and scraping them, XRD analyses of the recovered materials were conducted. It should be noted that the decrease of the S peaks with cycling was not only caused by the LiPS shuttle effect but also by some loss during washing.

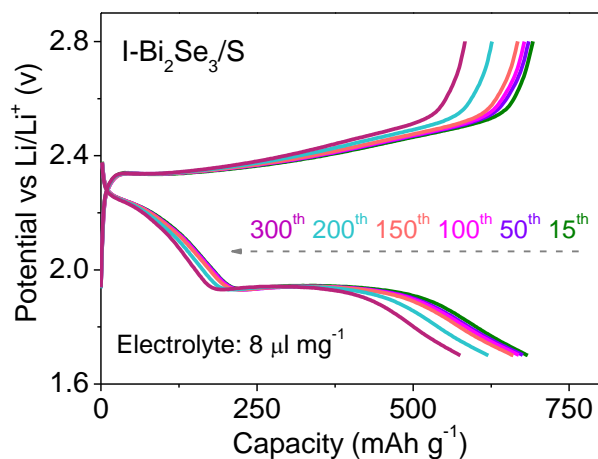


**Figure S17.** Galvanostatic charge/discharge profiles of I-Bi<sub>2</sub>Se<sub>3</sub>/S at 0.5C under a lean electrolyte condition with a high sulfur loading of 5.2 mg cm<sup>-2</sup>.

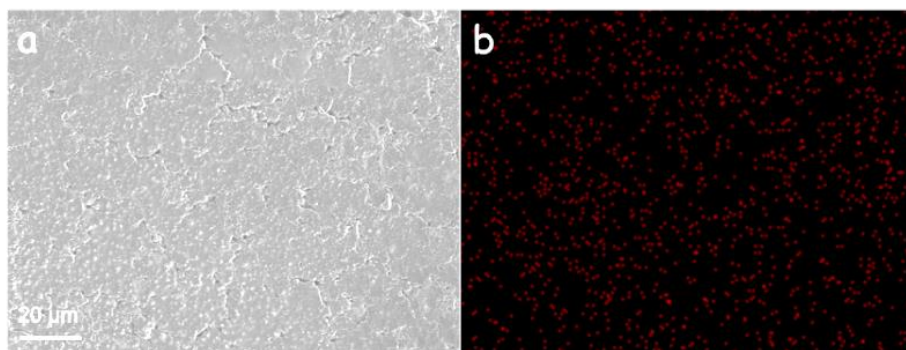


**Figure S18.** (a) SEM image of the Li-anode after cycling; (b) EDX mapping image of Li-anode showing sulfur signal after cycling.

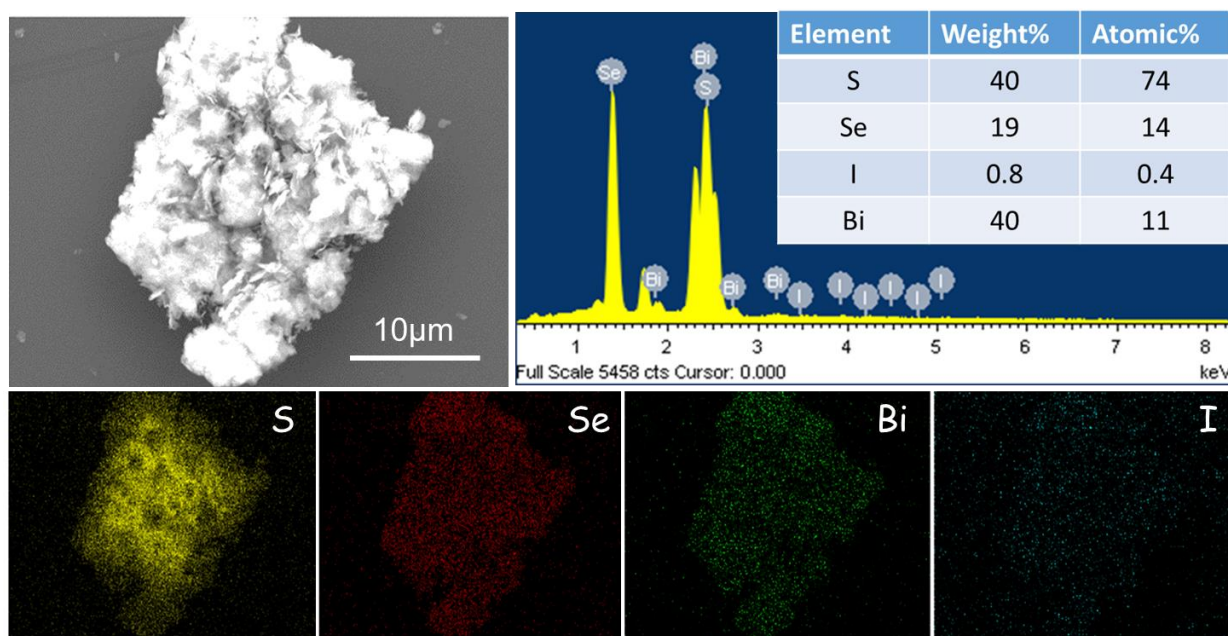


**Figure S19.** SEM image of the cathode material after cycling, EDX spectra and EDX elemental maps for S, Se, Bi and I. The at% of I with respect to Bi, is ca. 4%, which is within the error range of the I initially introduced.

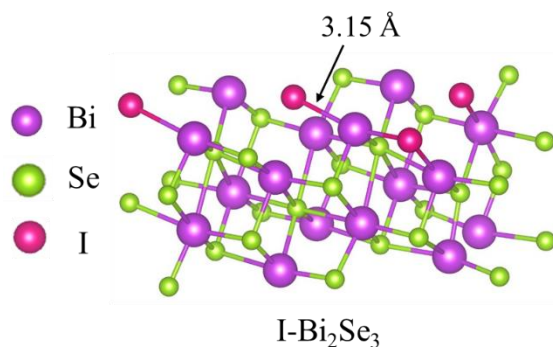


**Figure S20.** I-Bi<sub>2</sub>Se<sub>3</sub> optimized configuration as calculated by DFT. The distance between I and Bi is 3.15 Å, which is similar values than the bond lengths in bulk BiI<sub>3</sub>.

**Table S1** Summary of the comparison of I-Bi<sub>2</sub>Se<sub>3</sub> electrochemical performance as host cathode for LSBs with state-of-the-art Bi-based or Se-based materials.

Material	Capacity (mAh g <sup>-1</sup> ) (current rate)	Rate Capability (%) (current rate)	Bi/Se Content (%) (wt%)	Reference	
Bi <sub>2</sub> O <sub>3</sub> @Co/N-PC	1086 (0.25C)	70% (500, 1.5C)	0.06%	62.7%	[2]
Bi <sub>4</sub> Ti <sub>3</sub> O <sub>12</sub> /CNT	1256 (0.1C)	63% (1000, 1C)	0.037%	72.5%	[3]
BiOCl/G	1414 (0.1C)	85% (200, 0.2C)	0.05%	69%	[4]
Bi <sub>2</sub> S <sub>3</sub> HS	1051 (0.1C)	30% (500, 1C)	0.14%	64%	[5]
N-CN@Co <sub>3</sub> Se <sub>4</sub>	1437 (0.1C)	46% (800, 0.2C)	0.067%	61.5%	[6]
MoSe <sub>2</sub> @MoO <sub>2</sub>	1205 (0.1C)	77% (500, 0.5C)	0.046%	66%	[7]
u-NiCo <sub>2</sub> Se <sub>4</sub>	1330 (0.1C)	68.6% (2000, 3C)	0.016%	70%	[8]
Sb <sub>2</sub> Se <sub>3</sub> /rGO	1160 (0.2C)	71.5% (500, 1C)	0.057%	70%	[9]
CoZn-Se@N-MX	1270 (0.2C)	80% (100, 0.2C)	0.2%	70%	[10]
<b>I-Bi<sub>2</sub>Se<sub>3</sub></b>	<b>1496 (0.1C)</b>	<b>88% (1000, 1C)</b>	<b>0.012%</b>	<b>70.2%</b>	<b>Our work</b>

## References

- [1] D. Yang, Z. Liang, C. Zhang, J. J. Biendicho, M. Botifoll, M. C. Spadaro, Q. Chen, M. Li, A. Ramon, A. O. Moghaddam, J. Llorca, J. Wang, J. R. Morante, J. Arbiol, S. L. Chou, A. Cabot, *Adv. Energy Mater.* **2021**, *11*, 2101250.
- [2] H. Liu, Z. Chen, L. Zhou, X. Li, K. Pei, J. Zhang, Y. Song, F. Fang, R. Che, D. Sun, *J. Mater. Chem. A* **2019**, *7*, 7074–7081.
- [3] Y. Zhou, H. Shu, Y. Zhou, T. Sun, M. Han, Y. Chen, M. Chen, Z. Chen, X. Yang, X. Wang, *J. Power Sources* **2020**, *453*, 227896.
- [4] X. Wu, N. Liu, M. Wang, Y. Qiu, B. Guan, D. Tian, Z. Guo, L. Fan, N. Zhang, *ACS Nano* **2019**, *13*, 13109–13115.
- [5] B. Long, Z. Qiao, J. Zhang, S. Zhang, M. S. Balogun, J. Lu, S. Song, Y. Tong, *J. Mater. Chem. A* **2019**, *7*, 11370–11378.
- [6] D. Cai, B. Liu, D. Zhu, D. Chen, M. Lu, J. Cao, Y. Wang, W. Huang, Y. Shao, H. Tu, W. Han, *Adv. Energy Mater.* **2020**, *10*, 1904273.
- [7] Q. Hao, G. Cui, Y. Zhang, J. Li, Z. Zhang, *Chem. Eng. J.* **2020**, *381*, 122672.
- [8] C. Zhang, J. J. Biendicho, T. Zhang, R. Du, J. Li, X. Yang, J. Arbiol, Y. Zhou, J. R. Morante, A. Cabot, *Adv. Funct. Mater.* **2019**, *29*, 1903842.
- [9] Y. Tian, G. Li, Y. Zhang, D. Luo, X. Wang, Y. Zhao, H. Liu, P. Ji, X. Du, J. Li, Z. Chen, *Adv. Mater.* **2020**, *32*, 1904876.
- [10] Z. Ye, Y. Jiang, L. Li, F. Wu, R. Chen, *Adv. Mater.* **2021**, *33*, 2101204.